

Full paper



# Subambient daytime cooling enabled by hierarchically architected all-inorganic metapaper with enhanced thermal dissipation

Yanpei Tian<sup>a</sup>, Xiaojie Liu<sup>a</sup>, Ziqi Wang<sup>a</sup>, Jiansheng Li<sup>a</sup>, Ying Mu<sup>a</sup>, Shiyu Zhou<sup>b</sup>, Fangqi Chen<sup>a</sup>, Marilyn L. Minus<sup>a</sup>, Gang Xiao<sup>b</sup>, Yi Zheng<sup>a,\*</sup>

<sup>a</sup> Department of Mechanical and Industrial Engineering, Northeastern University, Boston, MA 02115, USA

<sup>b</sup> Department of Physics, Brown University, Providence, RI 02912, USA

## ARTICLE INFO

## Keywords:

Hydroxyapatite  
Solvothermal  
Inorganic metapaper  
Radiative cooling  
Biocompatibility  
Thermal dissipation

## ABSTRACT

Daytime radiative cooling shows great promise for cooling terrestrial objects without energy consumption. Intensive research has yielded numerous material candidates, such as nanophotonic structures and polymer-dielectric composites, however, challenges exist, ranging from the cost of nanofabrication for nanophotonic structures to environmental threats of micro and nanoplastics during polymer degradation under sunlight exposure. Moreover, the effect of a material's thermal conductivity on heat dissipation has been overlooked in the past. Herein, we report the synthesis and study of a hierarchical hydroxyapatite inorganic radiative cooling (HIRC) metapaper to simultaneously achieve efficient radiative cooling and enhanced thermal dissipation to accelerate heat release. We demonstrate that the HIRC metapaper is featured with high solar reflectance (0.99) and high mid-infrared thermal emittance (0.90) and it yields a subambient temperature drop of 5.1 °C under solar irradiance of 950 W m<sup>-2</sup> and a peak radiative cooling power of 104 W m<sup>-2</sup> under the solar intensity of 910 W m<sup>-2</sup> without polyethylene windshields. Moreover, the thermal conductivity of the metapaper exceeds that of polymer composites, thus enhancing the thermal dissipation from the underlying space. Furthermore, the hydroxyapatite's biocompatibility eliminates the concern of micro and nanoplastics release into the environment.

## 1. Introduction

Temperature regulation of infrastructures such as heating and cooling is a worldwide necessity for humanity which consumes 12% of global energy expense [1,2]. For cooling applications, the predominant compressor-based cooling systems (e.g., air conditioners) require stable supplies of electricity and associated coolants, stressing the environment due to the greenhouse effect or ozone-depletion gas emissions [3, 4]. Thus, energy-free and eco-friendly cooling alternatives are highly preferable over traditional energy-intensive cooling techniques [5,6]. One approach is radiative cooling, a passive and natural enhancement with zero energy consumption, for terrestrial objects to dissipate heat to the cold reservoir of outer space through the atmospheric window (8–13 μm) [7]. Owing to their high infrared emittance, organic and inorganic materials such as paints, dielectric layers, and metalized polymer coatings have been widely employed for nocturnal radiative cooling [8–10]. Daytime radiative cooling requires that a surface can reflect sunlight (0.3–2.5 μm) efficiently and radiates heat simultaneously. This spectral selectivity maximizes the net radiative cooling

power,  $P_{net}$ , defined by [11]:

$$P_{net} = I_{BB}(T)\bar{\epsilon} - I_{solar}(1 - \bar{R}) - h(T_{air} - T) - I_{BB}(T_{air})\bar{\epsilon}\bar{\epsilon}_{air} \quad (1)$$

where  $I_{BB}(T)$  and  $I_{BB}(T_{air})$  are the blackbody radiation heat flux of the cooling surface and ambient air with temperatures of  $T$  and  $T_{air}$ , respectively.  $I_{BB} = \sigma T^4$ , where  $\sigma$  is the Stefan–Boltzmann constant.  $I_{solar}$  stands for the standard irradiance flux of AM 1.5 (ASTM G173, 1000 W m<sup>-2</sup>),  $h$  represents the non-radiative heat transfer coefficient ( $2 \leq h \leq 10$  W m<sup>-2</sup> K<sup>-1</sup> under the natural air convection).  $\bar{\epsilon}$  and  $\bar{\epsilon}_{air}$  define the absorptance of the cooling surface and ambient air, respectively. Hemispherical emittance,  $\bar{\epsilon}$ , of the surface, equals 1 subtract hemispherical reflectance,  $\bar{R}$ , when an object is opaque. To enhance the cooling power, one effective route is architecting a surface that possesses an approaching unity solar  $\bar{R}$  for minimizing solar heating gain and a high  $\bar{\epsilon}$  for maximizing radiative heat loss [12,13]. The hemispherical  $\bar{R}$  and  $\bar{\epsilon}$  ensure that the cooling surface reflects sunlight from any angles of incidence and dissipates heat to any angles of the sky, respectively [14,15]. The gain of  $\bar{R}$  increasing by 1% is much higher than the 1% increase of  $\bar{\epsilon}$  since the standard solar irradiance

\* Corresponding author.

E-mail address: [y.zheng@northeastern.edu](mailto:y.zheng@northeastern.edu) (Y. Zheng).

<https://doi.org/10.1016/j.nanoen.2022.107085>

Received 23 September 2021; Received in revised form 12 February 2022; Accepted 20 February 2022

Available online 3 March 2022

2211-2855/© 2022 Elsevier Ltd. All rights reserved.

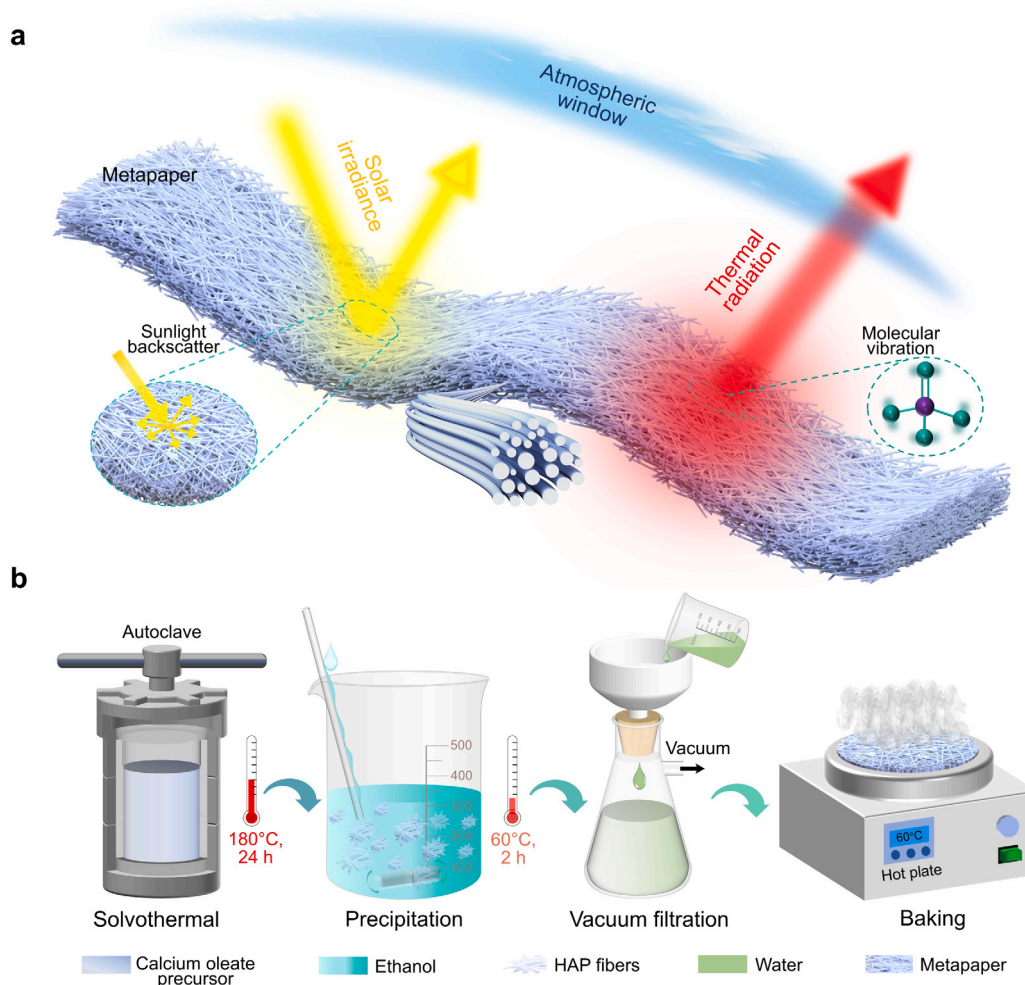


**Fig. 1.** Schematic illustrating the radiative cooling mechanism of the HIRC metapaper and its fabrication process. (a) HIRC metapaper with high  $\bar{R}$  and  $\bar{\epsilon}$  enables a net radiative heat loss. Effective sunlight backscattering of hierarchical HAP fibers of the HIRC metapaper yields high  $\bar{R}$  and molecular vibrations of chemical bonds in HAP fibers allow for high  $\bar{\epsilon}$ . (b) HAP fibers are synthesized by the calcium oleate solvothermal method and HIRC metapaper is prepared by vacuum-assisted suction filtration to form a paper sheet. The ethanol helps the precipitation of HAP fibers and the baking process accelerates the evaporation of ethanol and water.

( $1000 \text{ W m}^{-2}$ ) is much higher than that of the radiative heat flux ( $\approx 170 \text{ W m}^{-2}$ ) between a blackbody at 303 K, the outer space at  $\sim 3 \text{ K}$ , and the air at 303 K. Just a few percent drops of  $\bar{R}$  will render that the solar heating power exceeds the cooling power and this eventually heats the surface [16]. Another two generally overlooked aspects of radiative cooling materials are their thickness and thermal conductivity. The high  $\bar{R}$  and  $\bar{\epsilon}$  of the cooling materials cannot be presented when they are below a critical thickness [17]. Above the critical value, the extra thickness will introduce a large thermal resistance and then partially counteract the temperature reduction of cooling materials [18]. Thus, radiative cooling materials with high thermal conductivity are also desired to accelerate thermal dissipation from the underlying space.

Recently, a wide variety of structures and materials, such as dielectric nanophotonic structures [5,6,9], photonic polymers [11,16], polymer composites [15,17], and delignified wood [19] with high  $\bar{R}$  and  $\bar{\epsilon}$  have been demonstrated a subambient daytime radiative cooling achievement. However, the high cost of nanofabrication renders the nanophotonic approaches uneconomical for large-area commercial applications [6]. The photodegradation of polymers after long-term exposure to UV irradiation may release micro and nanoplastics into the global biosphere [20–23]. Microbial degradation of wood in damp and rainy weather might subvert its specific spectral property and cooling performance during a long life cycle [24]. Therefore, scalable, environmentally friendly, and weather-resistant photonic

metasurfaces with spectral selectivity are highly desirable for radiative cooling applications.

Hydroxyapatite (HAP),  $\text{Ca}_{10}(\text{OH})_2(\text{PO}_4)_6$ , is an abundant, biocompatible, and environmentally friendly biomaterial derived from the calcium phosphate family. It is a major inorganic constituent of bone and tooth of vertebrate and has been widely investigated for biomedical applications [25,26]. Compared with other morphologies of synthetic nanostructured HAP, such as nanoparticles [27], nanosheets [28], nanorods [29], and mesoporous microspheres [30] with poor flexibility, ultralong hydroxyapatite fibers (HAP fibers) with high aspect ratios have been synthesized through a solvothermal process and demonstrated as a promising biomaterial with high flexibility and thermal stability [31,32]. HAP fibers can self-assemble into bundles and intertwine to form a porous network, i.e., a paper sheet, which efficiently backscatters sunlight to show a high solar reflectance (Fig. 1a) [33]. Meanwhile, the strong molecular vibrations of phosphate radical ( $\text{PO}_4^{3-}$ ) offer high thermal emittance across the atmospheric window. This unique spectral selectivity renders hierarchical hydroxyapatite inorganic radiative cooling metapaper (HIRC metapaper) a promising alternative for radiative cooling implementations. In this study, it is demonstrated that efficient subambient daytime radiative cooling can be achieved by hierarchically architected all-inorganic metapaper. This metapaper consists of hierarchically structured HAP fibers which are fabricated by a one-pot calcium oleate precursor solvothermal method. The direct vacuum filtration method is employed to transform HAP fibers into

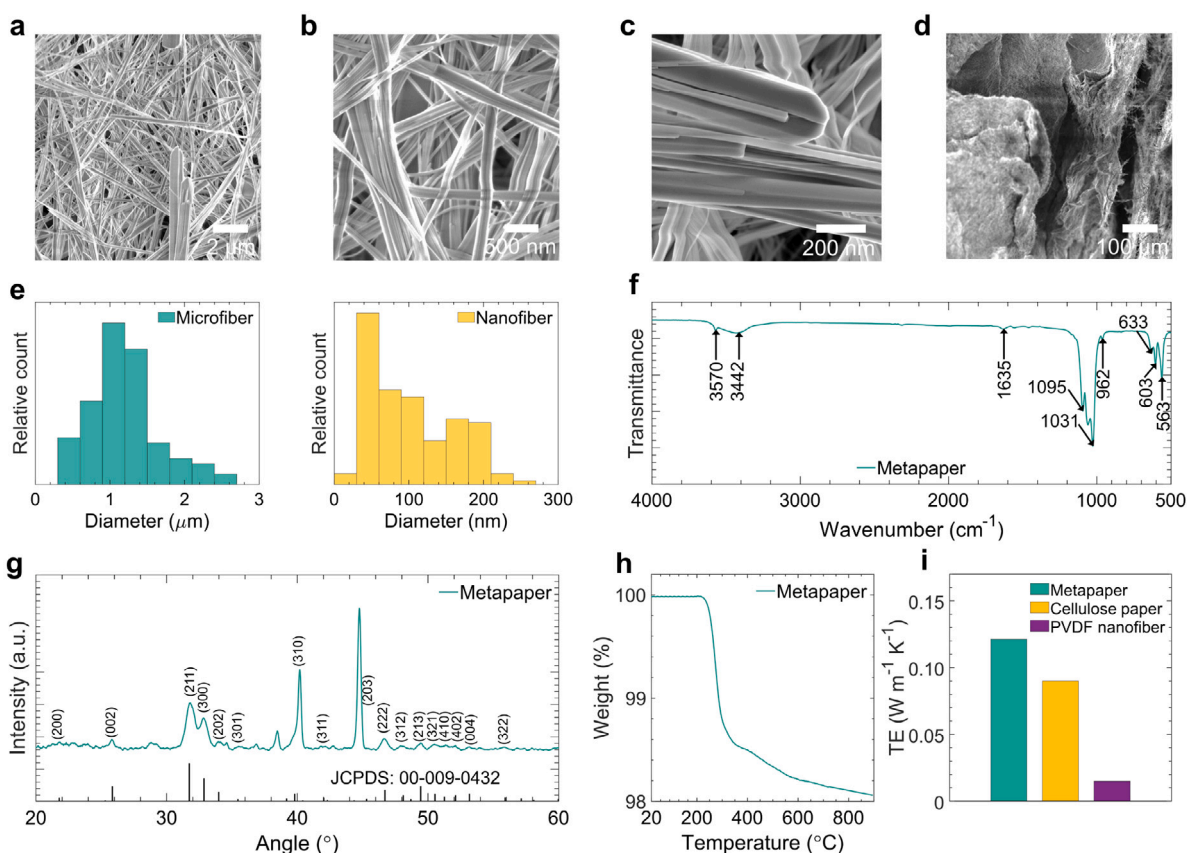


**Fig. 2. Material characterizations of HAP fibers.** (a–c) SEM images (top view) of the HIRC metapaper depicting its hierarchical structure. (d) SEM image (cross-section) of the HIRC metapaper. (e) Size distributions of nano and microfibers in HIRC metapaper showing weighted mean fiber sizes of  $\sim 50$  nm for nanofibers and  $\sim 1$   $\mu\text{m}$  for microfibers. (f) FTIR spectrum elucidating the chemical bonds of HAP fibers. (g) XRD pattern of HAP fibers that is consistent with patterns of JCPDS no. 00-009-0432. (h) TG curves of the HIRC metapaper. (i) Thermal conductivity of the HIRC metapaper compared with cellulose paper and PVDF nanofiber film.

a paper-like sheet with good flexibility. The HIRC metapaper exhibits excellent  $\bar{R}$  of 0.99 and  $\bar{\varepsilon}$  of 0.90 and results in superb radiative cooling performance, exemplified by a subambient temperature drop of 5.1  $^{\circ}\text{C}$  under solar irradiance of 950  $\text{W m}^{-2}$  and an average noontime (11:30 to 13:00) radiative cooling power of 80  $\text{W m}^{-2}$  under average solar irradiation of 860  $\text{W m}^{-2}$ . Different from those in previously reported work [13,16,19,34–37] that infrared-transparent polyethylene (PE) window shields are covered over radiative cooling materials to reduce the convection heating of air during the hot summer, our measured values are recorded when HIRC metapaper is directly exposed to strong solar irradiance and convection air heating. The relatively high thermal conductivity of the HIRC metapaper compared with other cooling polymer composites accelerates thermal dissipation from the underlying hot space. Moreover, the fire-retardancy of the HIRC metapaper alleviates fire safety concerns for building applications and the biocompatibility of HAP does not bring additional micro and nanoplastics pollution to the terrestrial ecosystems. With these advantages, the HIRC metapaper offers a new and superior material candidate for energy-efficient and environmentally-friendly subambient daytime cooling.

## 2. Results and discussion

### 2.1. Preparation and characterization of the HIRC metapaper

Briefly, the HIRC metapaper is fabricated starting from the synthesis of HAP fibers using the calcium oleate precursor consisting of  $\text{CaCl}_2$ , NaOH, oleic acid,  $\text{NaH}_2\text{PO}_4 \cdot 2\text{H}_2\text{O}$ , ethanol, and deionized (DI) water (Fig. 1b and Fig. S1a). After solvothermal reaction at 180  $^{\circ}\text{C}$  for 24 h, a stable wool-like HAP fiber suspension precipitates after the addition of 60  $^{\circ}\text{C}$  ethanol (Fig. S1b). Assisted by the vacuum filtration, HAP fibers

self-assemble into a free-standing layered metapaper with a thickness of  $\sim 500$   $\mu\text{m}$ , and the metapaper is in an ultra-white color contrasting with the underlying blackboard (Fig. S1c). The as-prepared HIRC metapaper shows good flexibility that can be bent easily for curved surfaces in real-life applications (Fig. S2). The following baking process accelerates the evaporation of ethanol and water. Furthermore, the thickness of the HIRC metapaper can be readily adjusted by varying the concentration or the mass of HAP fibers. 500  $\mu\text{m}$  thick HIRC metapaper can render a balance between high  $\bar{R}$ ,  $\bar{\varepsilon}$  and the flexibility, and this thickness is referred to the following sections unless otherwise specified. Large-area metapaper can be simply prepared by increasing the mass of raw chemicals for large-scale implementations. The wool-like HAP fiber suspension is similar to the paper pulp in the traditional cellulose-based paper production process. The manufacturing of the HIRC metapaper can be scaled up by the roll-to-roll paper production industry.

The as-prepared HIRC metapaper is composed of ultralong HAP fibers (200  $\mu\text{m}$ ) with diameters of 1  $\mu\text{m}$  (Fig. S3). The high-aspect-ratio HAP fibers self-assemble into the HIRC metapaper with a three-dimensional random porous network (Fig. 2a). High-magnification scanning electron microscope (SEM) micrographs show that nanoscale HAP fibers self-assemble parallelly into bundles to form an ultralong fiber (Fig. 2b, c, and Fig. S4). The HIRC metapaper exhibits a similar layer-staggered structure as the traditional cellulose paper as illustrated in the cross-section SEM micrographs (Fig. 2d and Fig. S5 and S6). HAP fibers' diameter measurement indicates that fiber diameters are bimodally and broadly distributed from 0.02 to 2.8  $\mu\text{m}$ , centered at  $\sim 50$  nm and  $\sim 1$   $\mu\text{m}$  for the nano and microfibers, respectively (Fig. 2e). These HAP fibers with diameters from the nanoscale to microscale are structured into a hierarchical form. Fourier transform infrared (FTIR) spectra elucidate characteristic absorption peaks of hydroxyl group

(3570 and 633  $\text{cm}^{-1}$ ),  $\text{PO}_4^{3-}$  (1095, 1031, 962, 603, and 563  $\text{cm}^{-1}$ ), and absorbed water (3442 and 1635  $\text{cm}^{-1}$ ) (Fig. 2f) [38,39]. The X-ray powder diffraction (XRD) pattern illustrates the ultralong HAP fibers are crystallized and identical to the standard XRD patterns of HAP (JCPDS no. 00-009-0432, Fig. 2g). Thermogravimetric analysis (TGA) curve of the HIRC metapaper shows that the oleate group decomposes at  $\sim 200$  °C (Fig. 2h). Above 600 °C, the weight of HAP almost keeps unchanged, illustrating its thermal stability at a high temperature up to 900 °C. The thermal conductivity of the metapaper is  $0.12 \text{ W m}^{-1} \text{ K}^{-1}$  which is higher than that of cellulose paper by 35% and PVDF nanofiber thin film by 700% in previously reported work about the radiative cooling application (Fig. 2i) [40,41]. The thermal conductivity of HIRC metapaper is high because the hydroxyapatite is inorganic material which shows higher thermal dissipation capability than organic materials such as cellulose and PVDF. Due to the highly porous property of HIRC metapaper, the encapsulated air as a thermal insulator reduces the thermal conductivity of the metapaper. Although the thermal conductivity of  $0.12 \text{ W m}^{-1} \text{ K}^{-1}$  is low compared with that of those thermal conductive materials such as metals and ceramic, the HIRC metapaper indeed shows a higher thermal conductivity than the porous organic films or fibers [17,41]. The tensile test result indicates that the HIRC metapaper has good mechanical strength for outdoor constructions (Fig. S7).

## 2.2. Optical properties, electrical field simulation, and heat transfer model

The measured spectral reflectance of the HIRC metapaper indicates that the 500  $\mu\text{m}$  thick film can reflect 98.6% solar irradiation while possessing a high thermal emittance of 0.90 between 8 and 13  $\mu\text{m}$  (Fig. 3a). The highly emissive wavelengths of the HIRC metapaper coincide with spectral irradiance peaks of the 303 K blackbody and atmospheric transparency wavelengths, ensuring efficient radiative heat loss in the form of infrared irradiation. Furthermore, the hierarchically randomized arranged HAP fibers result in a high and diffused  $\bar{R}$ , which strongly backscatters sunlight regardless of any angles of incidence (0–60°; Fig. 2e and Fig. 3b). For thermal wavelengths, an angle-independent high  $\bar{\epsilon}$  of 0.90 is demonstrated due to the strong molecular vibration peaks of  $\text{PO}_4^{3-}$  over the atmospheric transparency wavelengths (Fig. 2f and Fig. 3c). The HIRC metapaper shows both higher  $\bar{R}$  and  $\bar{\epsilon}$  than that of the HAP solid (Fig. S8), which is attributed to the hierarchically architected porous surface of the HIRC metapaper. This spectrally selective reflectance over solar and thermal wavelengths of the HIRC metapaper is intrinsically ideal for radiative cooling applications. The negligible extinction coefficient of HAP over most of the solar wavelengths (0.3–1.7  $\mu\text{m}$ ) reduces sunlight absorption to a minimum (Fig. 3d). Since the nanosized HAP fibers are bundled together, we simplify the structure of a single HAP fiber to be HAP gratings and calculate its complex refractive index (Fig. S9 and supplementary notes). The grating structure shows an even lower extinction coefficient than that of the solid HAP, which means a further reduction of the solar absorption. When architected into a hierarchical form, HAP fibers in microscale strongly scatter sunlight of all wavelengths, which is further enhanced by nanofibers over ultraviolet (UV) and visible wavelengths (Fig. 3e and Fig. S10). As corroborated by the absorption efficiency analysis, HAP fibers with diameters from 0.02 to 2.8  $\mu\text{m}$  show nearly no solar absorption (Fig. S11). To investigate photon scattering of the air voids and hierarchical nanofiber structure, finite-difference time-domain (FDTD) electrical field simulations of the HIRC metapaper ( $30 \times 10 \mu\text{m}$ ) are conducted (Fig. 3f and Fig. S12). The electrical field distributions corresponding to wavelengths of 0.3, 0.5, 1.0, and 1.7  $\mu\text{m}$  are selected as representative results for the solar wavelengths. The scattering effects of HAP fibers due to the abundant air voids and hierarchical fibers are clearly shown for all wavelengths, which is consistent with the scattering efficiency calculation. Scattering happens at the interface of air voids and fibers. The electric field of longer wavelengths propagates deeper than that of shorter wavelengths, and

the same tendency is also shown at the power density distribution (Fig. S13). The strong backscattering of air voids and hierarchical HAP fibers makes HIRC metapaper reflect much more sunlight than the commercial titanium dioxide ( $\text{TiO}_2$ ) white paint (Fig. S14).

Thermal conductivity and thickness are two key parameters affecting the thermal dissipation of radiative cooling materials (Fig. 3g). The only approach for the underlying heat source to dissipate heat through radiative cooling materials to the outside space is thermal conduction. As we discussed above, subambient radiative cooling is hard to achieve when there is an underlying heat source in real-life situations. Cooling materials with low thermal conductivity become thermal insulators to block thermal dissipation to the outside space. Fig. 3h, i depict the temperature difference,  $\Delta T = (T_{\text{bottom}} - T_{\text{top}})$ , of radiative cooling materials with different thermal conductivities and various thicknesses as a function of top surface temperature, where  $T_{\text{bottom}}$  and  $T_{\text{top}}$  are temperatures of the bottom and top surface of radiative cooling materials, respectively. Details of the heat transfer model are depicted in the supplementary notes. The thickness is fixed at 1 mm for results in Fig. 3h and the thermal conductivity is kept at  $0.05 \text{ W m}^{-1} \text{ K}^{-1}$  for data in Fig. 3i. It is demonstrated that the increased thermal conductivity or thickness will partially cancel out the temperature drop of the top surface of radiative cooling materials. Therefore, the relatively high thermal conductivity of the HIRC metapaper benefits the thermal dissipation of the heat source in the underlying space.

## 2.3. Daytime radiative cooling performance of the HIRC metapaper

The selective high infrared thermal emittance is designed for achieving maximum subambient cooling since it can reduce the thermal radiative heating effect from the hot ambient, even though this reduces the net radiative cooling power. While the broadband high thermal emittance across the whole infrared range shows an advantage for thermal dissipation for an object with a temperature higher than the ambient and it offers a higher net radiative cooling power, it does not mean that the thermal emitter with broadband high thermal emittance cannot yield a subambient radiative cooling temperature drop. Regarding the HIRC metapaper investigated here, it shows an approaching unity (0.99) solar reflectance which has reduced the solar heating effect to a minimum. For applications when a maximum subambient temperature drop is desired, the net radiative cooling power might be compromised to design a surface with selective emittance. Due to its intrinsic infrared radiative property of HIRC metapaper, it does not indicate a surface with selective high thermal emittance across the atmospheric window. Subambient temperature drop and radiative cooling power measurements have been employed in previous work to evaluate the radiative cooling performance of materials. Inset of Fig. 4a schematically illustrates the structure inside the chamber and details about the experimental setup can be found in the experimental section. The steady-state temperature of the HIRC metapaper was measured in the first chamber, in which the Kapton heater was turned off (Fig. S15). The radiative cooling power of the HIRC metapaper was recorded in the second chamber, in which the Kapton heat was controlled by a proportional integral derivative (PID) feedback heating system, and the temperature of the HIRC metapaper was tracked to the ambient air. A wood sheet was selected in the third chamber as a control group to demonstrate the cooling ability of the HIRC metapaper. A weather station was used to monitor the wind speed, solar intensity, and relative humidity during the experiment period (Fig. S16). No infrared-transparent PE windshields were used to reduce the convection heating from ambient air, which is more in line with the practical application scenarios. The average solar intensity during the experimental period was  $\sim 860 \text{ W m}^{-2}$  (Fig. 4b) and the average wind speed was  $\sim 7.0 \text{ km h}^{-1}$  (Fig. 4c). The temperature tracking result (Fig. 4d) and the distribution of temperature difference and cooling power (Fig. S17 and S18) demonstrate the reliability of the real-time measurement systems. In the noontime, the HIRC metapaper shows a

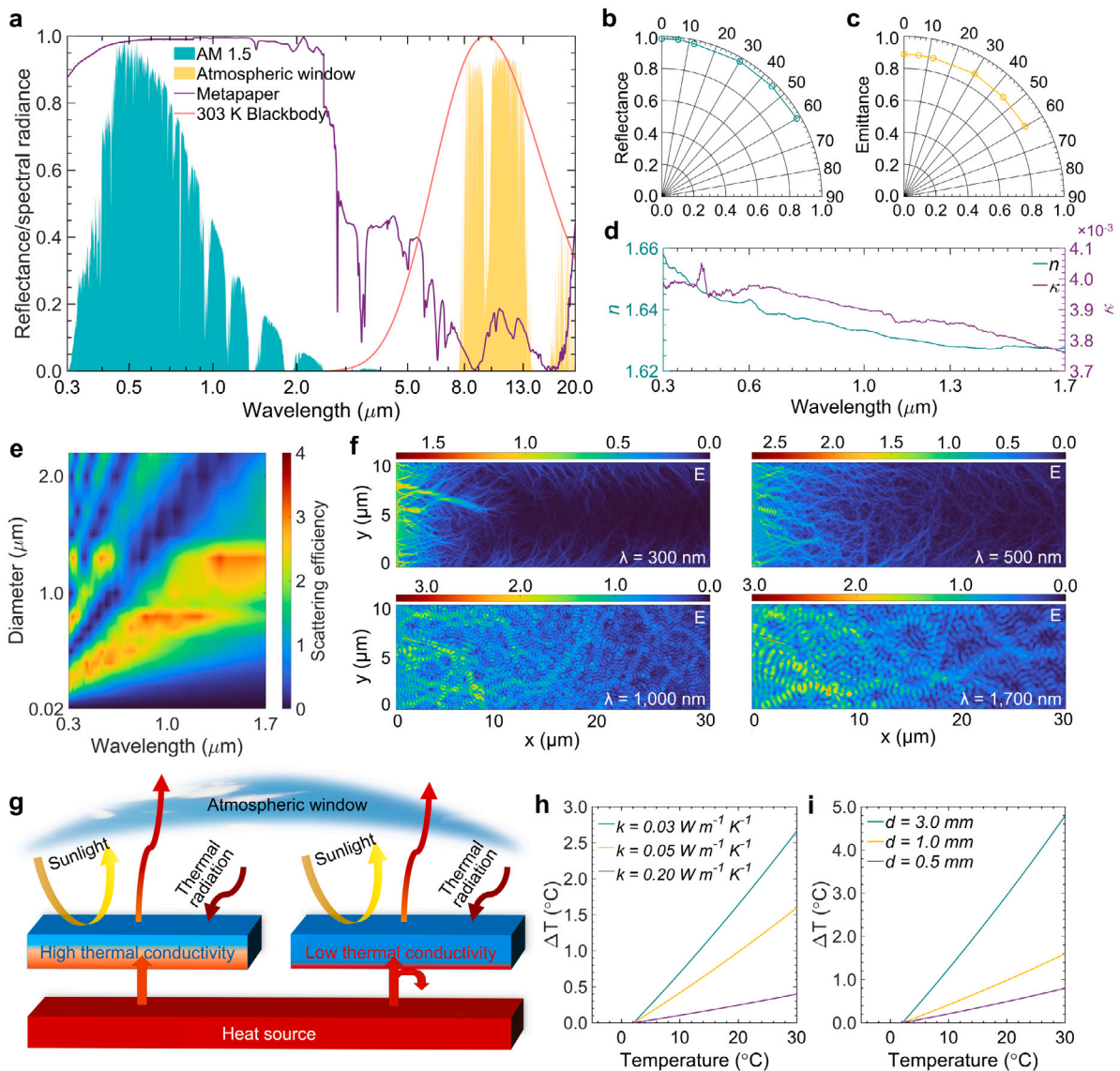


**Fig. 3.** Optical, FDTD simulation, and enhanced thermal dissipation analysis of the HIRC metapaper. (a) Hemispherical spectral reflectance of a 500  $\mu\text{m}$  thick HIRC metapaper displaying against the normalized AM 1.5 spectrum (ASTM G173), the atmospheric window, and the normalized spectral irradiance of the 303 K blackbody. (b) High solar absorptance and (c) thermal emittance of the HIRC metapaper across angles. (d) Measured complex refractive index ( $n + ik$ ) of HAP fibers. (e) Simulated scattering efficiency of HAP fibers with sizes varying from 0.02 to 2.2  $\mu\text{m}$ . (f) Propagated electrical field simulations of the HIRC metapaper for the incident wavelengths of 300, 500, 1000, and 1700 nm. (g) Schematic illustrating the radiative and conductive heat transfer of radiative cooling materials with high and low thermal conductivity. The temperature difference between the top and bottom surfaces with (h) different thermal conductivities and (i) varying thicknesses as a function of temperatures of the materials.

subambient temperature drop of  $\sim 5.1$   $^{\circ}\text{C}$  under a solar intensity of  $950 \text{ W m}^{-2}$  and a peaking radiative cooling power of  $104 \text{ W m}^{-2}$  under direct solar irradiance ( $910 \text{ W m}^{-2}$ , Fig. 4e). Even though the removal of PE windshields will weaken the cooling performance, the cooling ability of the HIRC metapaper is still better or on par with other high-performance results in the literature (Table S1) [19,34,36,42,43]. The average temperature of wood as a control group is  $7.4$   $^{\circ}\text{C}$  higher than that of the HIRC metapaper. Fig. 4f shows the photograph and thermal image of wood and HIRC metapaper fixed on top of polystyrene (PS) foam under direct solar irradiance, the center temperature of the HIRC metapaper is  $13$   $^{\circ}\text{C}$  lower than that of the wood. These temperature differences illustrate the advantageous cooling capability of the HIRC metapaper. The experimental setups of Fig. 4d and f are different. Wood and metapaper samples in Fig. 4d are encapsulated inside the PS foam chamber and their backs are well insulated, while wood and metapaper samples in Fig. 4f are adhered on a PS foam with their sides exposed to the ambient. Moreover, the wood and metapaper in Fig. 4d are horizontally faced to the sky, while those in Fig. 4f are faced to the sun

at an angle of  $30^{\circ}$ . The temperatures of samples in Fig. 4f are higher than those of Fig. 4d because the side heating effect of ambient hot air and the oblique angle of the PS foam platform in Fig. 4f makes the solar irradiance intensity of Fig. 4f is higher than that of Fig. 4d.

The ambient convection and atmospheric transmittance are both of great significance to the radiative cooling performance (Fig. 4g, h). Ambient convection depends on the wind speed and ambient temperature. Here, we simulated the cooling power as a function of the HIRC metapaper's temperature under different convection conditions and atmospheric transmittance, and the ambient temperature is set to be  $30$   $^{\circ}\text{C}$ . With the increase of the HIRC metapaper's temperature, the cooling power goes up to maximum when temperatures of the HIRC metapaper and ambient are equal (Fig. 4g). This is because the non-radiative heating term becomes zero after temperatures of the HIRC metapaper and ambient are equal according to Eq. (1). Non-radiative heat transfer coefficient plays a key role in the cooling power, exemplified by that the radiative cooling powers are 79, 54, and  $29 \text{ W m}^{-2}$  corresponding to non-radiative heat transfer coefficients of 0, 5,

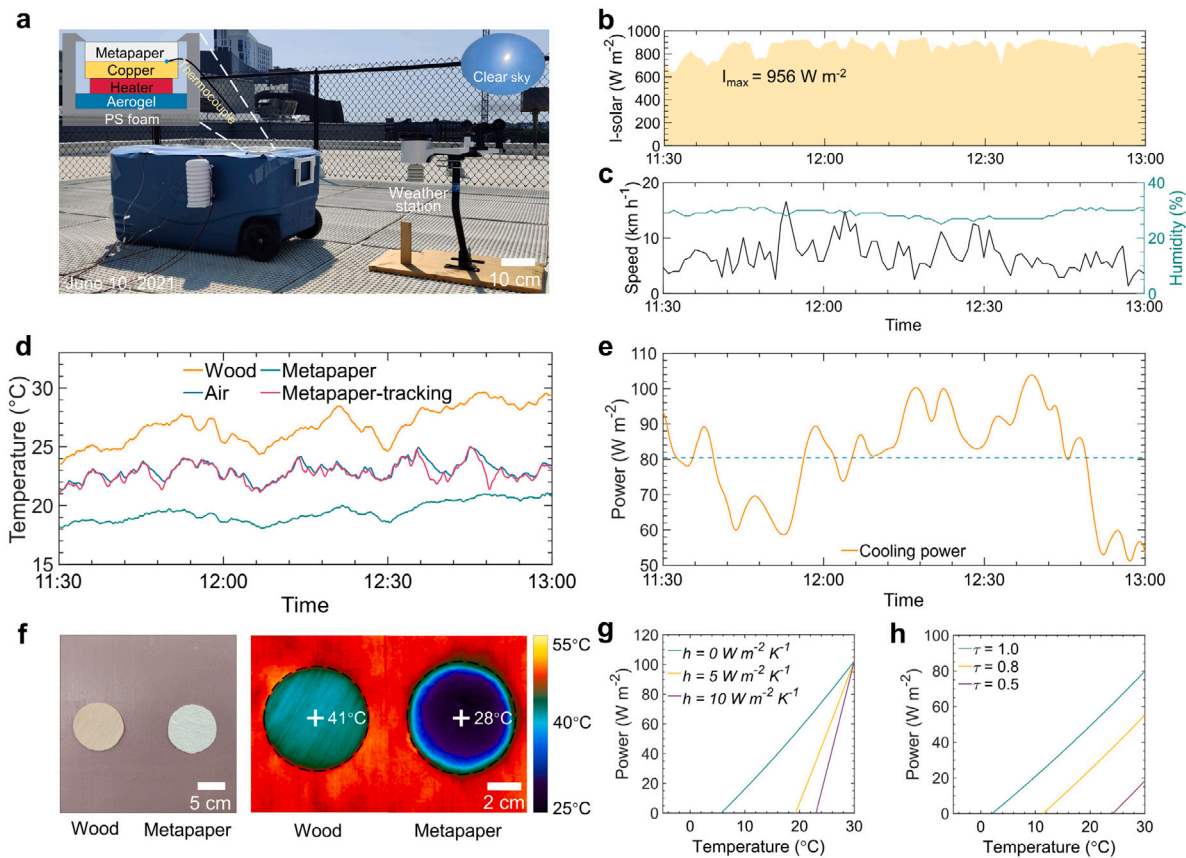


**Fig. 4. Outdoor radiative cooling performance evaluation of the HIRC metapaper.** (a) Photograph superimposed with schematic to show the setup of real-time measurement of radiative cooling performance (Boston, MA, USA, 42.36° N, 71.06° W, Jun 10, 2021). (b) Solar intensity variations, (c) wind speed, and relative humidity during the experimental period. (d) Temperature response of the wood, HIRC metapaper, and ambient air. The temperature data of the HIRC metapaper tracking to the air during the noontime. (e) The measured radiative cooling power of the HIRC metapaper. (f) Photograph (left) and infrared image (right) of wood and HIRC metapaper attached on PS foam under direct sunlight at noontime. The radiative cooling power of the HIRC metapaper under (g) different convection conditions and (h) various atmospheric transmittance as a function of the HIRC metapaper's temperature.

and  $10 \text{ W m}^{-2} \text{ K}^{-1}$ , respectively. A more important external factor is atmospheric transmittance that is directly dependent on weather conditions (i.e., humidity). We set the average transmittance,  $\tau$ , calculated using the extract atmospheric transmittance from MODTRAN 4 as 1. As illustrated in Fig. 4h, the cooling power decreases from 78 to  $17 \text{ W m}^{-2}$  when the average transmittance changes from 1 to 0.5.

#### 2.4. Fire and weather resistance of the HIRC metapaper

The fire retardancy of cooling materials for buildings is substantial to human safety [44]. Wood and concrete are two common and widely used construction materials. We test the flammability of the HIRC metapaper and compared it with wood and concrete, as the latter two are common building materials (Fig. 5a, b and Fig. S19). The combustion process of these materials was recorded after igniting by a blue torch with a flame temperature of  $\sim 1430 \text{ }^\circ\text{C}$ . The wood was easily burnt into ashes within 15 s, while no visual change appeared on the surface of the HIRC metapaper under the flame continuously for 15 s. A scorching hot spot appeared on the surface of the HIRC metapaper under a digital camera and infrared thermal camera (Fig. 5b, c, and Video S1). There is an obvious trace of burning on the concrete surface after 15 s burning of flames, while no trace of burning is observed on the surface of the HIRC metapaper. This demonstrates that HIRC metapaper is fire-retardant and safe for the application as building exteriors.

The fire-retardant test demonstrates the short-term fire resistance of HIRC metapaper under a high-temperature flame, but long-term (1 h) and high-temperature ( $>400 \text{ }^\circ\text{C}$ ) thermal stability is another key

parameter for HIRC metapaper to be fire-retardant. Therefore, 1 h thermal stability tests at various temperatures in an air environment are performed to demonstrate the long-term fire resistance. After each test, the solar reflectance and thermal emittance are measured to evaluate the thermal stability. The solar reflectance slightly reduces from 0.99 to 0.96, while the thermal emittance reduces from 0.9 to 0.83 after heating at  $1000 \text{ }^\circ\text{C}$  for 1 h. Overall, it shows that the  $\bar{R}$  and  $\bar{\epsilon}$  of the HIRC metapaper hold after high temperature up to  $800 \text{ }^\circ\text{C}$  (Fig. 5d). FTIR transmittance spectra validate that the chemical compositions of the HIRC metapaper keep no change after high temperature up to  $1000 \text{ }^\circ\text{C}$  (Fig. 5e). This elucidates that hydroxyapatite fibers do not decompose at such a high temperature. Therefore, the  $\bar{R}$  drops at  $1000 \text{ }^\circ\text{C}$  for 1 h might result from the size distribution change of HAP fibers (Fig. 5f and Fig. S20). Fiber diameter measurements indicate that the distribution becomes narrower and mean diameters turn smaller, which reduces the scattering efficiency of the broadband solar wavelengths (Fig. S21). Even though there is a small decrease in thermal emittance after thermal annealing at  $1000 \text{ }^\circ\text{C}$  for 1 h, its main radiative cooling performance remains high after the high-temperatures tests. Moreover, rare demonstrations about the fire resistance and thermal stability of radiative cooling materials were reported before. The fire-retardancy of the HIRC metapaper ensures its survivability after a fire and indicates its potential application of refractory insulation materials in the form of aerogel. Another key issue that affects the radiative cooling performance of HIRC metapaper is the dust in the air for outdoor applications. To validate this potential problem, a 7-day outdoor exposure experiment in Boston from January 08, 2022, to January 14, 2022, has been conducted. The metapaper and print paper

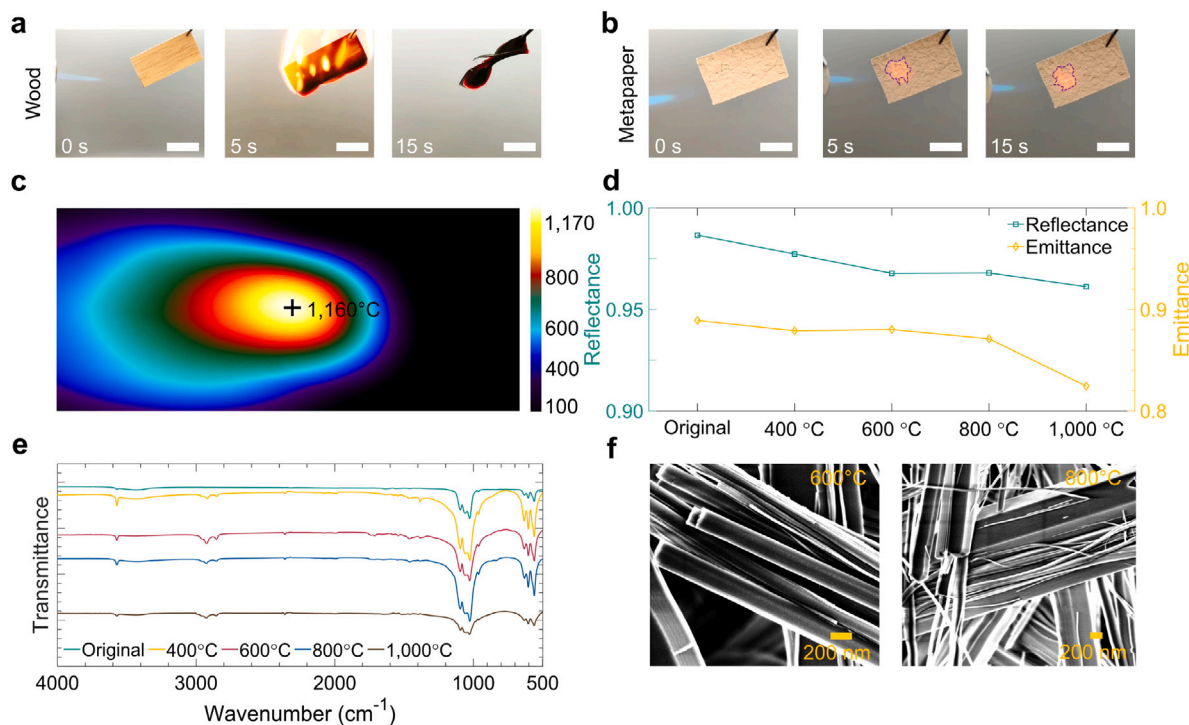


**Fig. 5.** Fire resistance and thermal stability of the HIRC metapaper. Fire-retardant tests of (a) wood and (b) HIRC metapaper. Dashed purple curves circles out the scorching hot spot of flame on the HIRC metapaper. (c) Infrared thermal image of the HIRC metapaper under the flame of a blue torch. (d) Overall  $\bar{R}$  and  $\bar{\epsilon}$  of the HIRC metapaper after thermal treatments at high temperatures for 1 h. (e) FTIR transmittance of the HIRC metapaper after high-temperature treatment for 1 h in the air at 600 °C and 800 °C.

(the control group) were secured by transparent tapes on the PS foam board and placed in outdoors ambient environment during the ambient temperature is around  $-2.5$  °C (Fig. S22–S23). No obvious changes are observed on the top surfaces of the metapaper sample. The reflectance spectra of the metapaper are consistent with the pristine one, which ensures its radiative cooling performance (Fig. S24). Overall, rare dust is settled on the metapaper surface from the SEM images (Fig. S25). When zoomed in, dust with a size of around  $50$   $\mu\text{m}$  is found. Due to the ultrawhite instincts, little reductions of the solar reflectance occur.

### 3. Conclusions

In conclusion, we have demonstrated all-inorganic hydroxyapatite metapaper with photonic architectures for subambient daytime radiative cooling application fabricating by a solvothermal process. The metapaper shows a high reflectance over broadband solar wavelengths because of its efficient backscattering occurring within innumerable hierarchical randomized photonic nanofibers and it also has a high thermal emittance overlapping the atmospheric transparency window due to its specific molecular bond vibrations. Furthermore, the added feature of a high thermal conductivity enhances thermal dissipation from the underlying space to the top metapaper surface. Both theoretical calculations and real-time measurements validate the excellent subambient cooling performance of this HIRC metapaper under a high solar flux ( $950$   $\text{W m}^{-2}$ ) without any convection windshields to undermine environmental convection heat gain. The HIRC metapaper is featured with a high solar reflectance of  $0.99$ , a high mid-infrared thermal emittance of  $0.90$ , a subambient temperature drop of  $5.1$  °C under a solar intensity of  $950$   $\text{W m}^{-2}$ , and a peak radiative cooling power of  $104$   $\text{W m}^{-2}$  under direct solar irradiance of  $910$   $\text{W m}^{-2}$ . This all-inorganic metapaper offers a viable pathway for the substantial reduction of energy consumption and alleviating the growing crisis of global warming. In addition, the biocompatibility of hydroxyapatite provides a new route for achieving high-performance radiative cooling

without releasing microplastics into the environment and it may inspire more radiative cooling composites purely from biodegradable and biocompatible substances towards an energy-efficient and sustainable society.

## 4. Experimental section

### 4.1. Materials

Calcium chloride ( $\text{CaCl}_2$ , anhydrous,  $\geq 97\%$ ), sodium hydroxide ( $\text{NaOH}$ ,  $\geq 97\%$ ), sodium dihydrogen phosphate ( $\text{NaH}_2\text{PO}_4 \cdot 2\text{H}_2\text{O}$ , anhydrous,  $\geq 97\%$ ), and oleic acid ( $\text{C}_{18}\text{H}_{34}\text{O}_2$ , natural, FCC) were kindly provided by Sigma-Aldrich. Denatured alcohol was provided by Lab Alley. Copper sheet, Kapton thin-film heater, thermocouples, and PS thermal insulation foam were purchased commercially from Amazon. Aerogel blanket was obtained from the Aerogel Technologies, LLC. The white paint (Rust-Oleum) was provided by Amazon.

### 4.2. Synthesis of the ultralong HAP fibers

HAP fibers were synthesized by the calcium oleate precursor solvothermal method. Oleic acid ( $72.00$  g) and denatured alcohol ( $72.00$  g) were mixed under vigorous mechanical agitation for  $20$  min. Then  $\text{CaCl}_2$  ( $1.32$  g) solution ( $100.00$  ml),  $\text{NaOH}$  ( $6.00$  g) solution ( $100.00$  ml), and  $\text{NaH}_2\text{PO}_4 \cdot 2\text{H}_2\text{O}$  ( $1.68$  g) solution ( $60.00$  ml) were consecutively dropwise added into the mixture of oleic acid and denatured alcohol. The above mixture was moved into a Teflon-lined stainless steel autoclave reactor ( $500.00$  ml) and solvothermal reacted at  $190$  °C for  $24$  h.

### 4.3. Fabrication of the HIRC metapaper and HAP solid sample

The obtained HAP fibers ( $\sim 450$  ml) were dispersed into denatured alcohol ( $500$  ml,  $60$  °C) under slow mechanical agitation ( $\sim 100$  r/min)

for 2 h to generate the HAP fibers suspension and remove the impurities. The as-prepared HAP fibers suspension was washed assisted by vacuum filtration to remove the alcohol. Then it was washed by 1 L deionized (DI) water (60 °C) to further remove residual impurities and alcohol under vacuum suction filtration and finally formed a paper-like sheet. The HIRC metapaper was obtained after drying on a 60 °C hot plate for 0.5 h. The HAP solid sample was prepared by mixing the HAP nanoparticles (~100 nm in diameter) with DI water and the weight ratio of HAP nanoparticles over DI water is 2:1 and then hydraulically pressed in a mold at 20 MPa for 5 min. The obtained HAP solid was thermally annealed at 600 °C in an air environment for 2 h.

#### 4.4. Fabrication of the outdoor radiative cooling experimental setup

The HIRC metapaper with a diameter of 10 cm and a thickness of 500  $\mu\text{m}$  was glued to a copper sheet (10 cm in diameter and thermal conductivity, 380  $\text{W m}^{-1} \text{K}^{-1}$ ) with the silver thermal compound paste (8.5  $\text{W m}^{-1} \text{K}^{-1}$ , Fig. S15). The copper sheet was stuck to the Kapton thin-film heater with a diameter of 10 cm in diameter and 400  $\mu\text{m}$  in thickness. The heater was placed on a 6 mm aerogel blanket (23  $\text{mW m}^{-1} \text{K}^{-1}$ ). A PS thermal insulation foam with thermal conductivity of 30  $\text{mW m}^{-1} \text{K}^{-1}$  with a thickness of 25 mm was used as the insulation chamber wall. All the above setup was sealed into a cooler box. The wood sheet (10 cm in diameter and 0.6 mm in thickness) also adhered to the same copper sheet. K-type thermocouples are adhered to the back of samples (HIRC metapaper and wood sheet) to measure their real-time temperature responses and these thermocouples are connected to the National Instruments (NI) PXI-6289 multifunction I/O module to record temperature data. The temperature tracking of the HIRC metapaper to the ambient was performed by switching between the “On” and “Off” states of the thin film heater controlled by the NI PXI-2586 relay module. These actions were driven by an NI LabVIEW-based program based on the PID control algorithm. The feedback-controlled algorithm kept the electrical heater to intermittently heat samples so that the temperature difference between the ambient and sample was less than 0.5 °C over the experimental period. The heating power generated by the electric heater offsets the radiative cooling power from the metapaper. When the temperature difference between the ambient and sample was within 0.5 °C, the electric heating power can be considered as the radiative cooling power of the metapaper.

#### 4.5. Materials characterizations

The surface morphologies of the HIRC metapaper were characterized using the SEM (Zeiss Supra) with an acceleration voltage of 3 kV. The size distribution of HAP fibers was measured by analyzing SEM images with the ImageJ software. The phase identifications of the HAP were conducted with an XRD (Bruker D8) scanning from 20 to 60° at a stepsize of 0.02°. The TG analysis was characterized by the TA Q50 from 20 to 900 °C under an airflow of 60  $\text{ml min}^{-1}$  with a temperature rising rate of 10 °C  $\text{min}^{-1}$ . Characterization of thermal conductivity was performed by the Hot Disk TPS 2500 S. Infrared images were recorded by a thermal camera (FLIR A655c). Complex refractive indices of the HIRC metapaper were measured using the ellipsometer (J.A. Woolam, M200DI) from 0.3 to 1.7  $\mu\text{m}$ . Hydroxyapatite fiber samples were put into a ball milling machine for 2 h to get nanoparticle powders, then the size of hydroxyapatite nanoparticles was milled down to 100 nm. The hydroxyapatite nanoparticles were hydraulically pressed under 30 MPa to form a pellet with a thickness of 1 mm and a diameter of 7 mm. The surface of hydraulic press dies was polished to mirror-like to reduce the surface roughness of hydroxyapatite pellet, that reduces the light scattering effect on its surface and increases the signal intensity.

#### 4.6. Optical characterizations

The hemispherical reflectance spectra of the HIRC metapaper were measured by a spectrophotometer (Jasco V770) over the UV–visible–near-IR (0.3–2.5  $\mu\text{m}$ ) wavelengths. The hemispherical reflectance spectra were characterized employing the FTIR spectrometer (Jasco 6600) over the mid-IR (2.5–20  $\mu\text{m}$ ) wavelengths. The  $\bar{\alpha}$  equals  $1 - \bar{R}$  since the transmittance ( $T$ ) of the HIRC metapaper at a thickness of 500  $\mu\text{m}$  is zero. The hemispherical absorptance is equal to the hemispherical emittance when an object is in thermodynamic equilibrium. Hemispherical reflectance spectra of the HIRC metapaper at varying angles of incidence were measured by using the home-built wedge block of diverse angles and following the same measurement procedures in our recent work [45]. The FTIR spectra were also examined by the Jasco FTIR 6600. The solar reflectance spectra and FTIR transmittance spectra were characterized after thermal treatment at high temperatures for 1 h.

#### 4.7. Fire-retardant and thermal stability experiment

The fire-retardant experiment was conducted by igniting the HIRC metapaper (3 cm  $\times$  2 cm  $\times$  500  $\mu\text{m}$ ) by a blue torch with a flame temperature of ~1430 °C for 15 s and recording its fire response by a camera. The wood sheet with the same size was selected as a control group and the igniting time of the wood sample was shortened to 1 s. The thermal stability experiment was performed by heating HIRC metapaper at various temperatures (400, 600, 800, and 1000 °C) for 1 h in an air environment using an alumina tube oven.

#### 4.8. Calculation of the overall solar absorptance and thermal emittance

The overall hemispherical solar reflectance,  $\bar{R}$ , is functions of wavelengths and incident angles, which is expressed as [45]:

$$\bar{R}(\lambda, \theta, \phi) = \frac{\int_{0.3\mu\text{m}}^{2.5\mu\text{m}} I_{\text{solar}}(\lambda, \theta, \phi) R(\lambda, \theta, \phi) d\lambda}{\int_{0.3\mu\text{m}}^{2.5\mu\text{m}} I_{\text{solar}}(\lambda, \theta, \phi) d\lambda} \quad (2)$$

where  $\lambda$  is the wavelength of the solar radiation,  $\phi$  is the azimuthal angle, and  $\theta$  is the polar angle.  $R(\lambda, \theta, \phi)$  is the spectral directional reflectance.

The overall hemispherical thermal emittance,  $\bar{\epsilon}$ , is also function of the wavelengths and incident angles, which is defined by [45]:

$$\bar{\epsilon}(\lambda, \theta, \phi) = \frac{\int_{2.5\mu\text{m}}^{20\mu\text{m}} I_{\text{bb}}(\lambda, \theta, \phi) [1 - R(\lambda, \theta, \phi)] d\lambda}{\int_{2.5\mu\text{m}}^{20\mu\text{m}} I_{\text{bb}}(\lambda, \theta, \phi) d\lambda} \quad (3)$$

where  $I_{\text{bb}}(\lambda, \theta, \phi)$  means the blackbody radiation intensity described by Planck's law.  $\bar{\epsilon}(\lambda, \theta, \phi)$  is the spectral directional absorptance at a certain operating temperature.

#### 4.9. FDTD optical simulation

The scattering efficiency of HAP fibers was executed using the Lumerical FDTD Solution 2018a. A two-dimensional (2D) FDTD model was simulated, and a total-field scattered-field wave source coupled with the HIRC metapaper was employed to simulate the scattering efficiency. The HAP fibers were assumed to be a square with side lengths varying from 0.02 to 2.2  $\mu\text{m}$ . The electrical and power field distributions of the HIRC metapaper (30  $\times$  10  $\mu\text{m}$ ) over the wavelength of 0.3–1.7  $\mu\text{m}$  were simulated in a 2D FDTD model with a plane wave source. The randomized air-void structures were generated with dimensions of 30  $\times$  10  $\mu\text{m}$  in the  $x$ - and  $y$ -direction by converting the grayscale SEM images of the HIRC metapaper into binary images using the MATLAB R2020a (MathWorks, Inc.). The processed 2D images of randomized air-voids structures were imported into Lumerical FDTD solution as the refractive index profile. The perfectly matched layer (PML) boundary conditions were employed to absorb all the outgoing

electromagnetic radiation. A plane wave source over wavelengths from 0.3 to 1.7  $\mu\text{m}$  was launched at a distance of 5  $\mu\text{m}$  away from the left edge of the HIRC metapaper simulation region and the refractive index of air voids was assigned as 1.

#### 4.10. Absorption efficiency calculation

The absorption efficiency of HAP fibers,  $\delta_{abs}$ , was defined by [46]:

$$\delta_{abs} = \frac{8\pi}{3} k^4 r^4 \left| \frac{\epsilon - \epsilon_m}{\epsilon + 2\epsilon_m} \right|^2 \quad (4)$$

where,  $k = 2\pi/\lambda$  represents the wave vector, and  $\lambda$  means the wavelength.  $r$  defines the radius of the nanoparticles.  $\epsilon$  is the complex dielectric function of the HAP and  $\epsilon_m$  is the dielectric constant of the surrounding medium (air).

#### CRedit authorship contribution statement

**Yanpei Tian:** Conceptualization, Data analysis, Writing – original draft, Experimentation design. **Xiaojie Liu:** Conceptualization, Data analysis. **Ziqi Wang:** Experimentation design. **Jiansheng Li:** Sample preparation, Experimental measurement. **Ying Mu:** TGA characterization. **Shiyu Zhou:** XRD characterization. **Fangqi Chen:** Sample preparation, Experimental measurement. **Marilyn L. Minus:** Data analysis, Review & editing. **Gang Xiao:** Data analysis, Review & editing. **Yi Zheng:** Supervision, Resources, Writing – review & editing.

#### Declaration of competing interest

The authors declare that they have no known competing financial interests or personal relationships that could have appeared to influence the work reported in this paper.

#### Acknowledgment

This project is supported by the National Science Foundation, USA through grant number CBET-1941743.

#### Appendix A. Supplementary data

Supplementary material related to this article can be found online at <https://doi.org/10.1016/j.nanoen.2022.107085>.

#### References

- [1] A. Henry, R. Prasher, A. Majumdar, Five thermal energy grand challenges for decarbonization, *Nat. Energy* 5 (9) (2020) 635–637.
- [2] M. Burke, S.M. Hsiang, E. Miguel, Global non-linear effect of temperature on economic production, *Nature* 527 (7577) (2015) 235–239.
- [3] T.L. Frölicher, E.M. Fischer, N. Gruber, Marine heatwaves under global warming, *Nature* 560 (7718) (2018) 360–364.
- [4] T.P. Hughes, J.T. Kerry, A.H. Baird, S.R. Connolly, A. Dietzel, C.M. Eakin, S.F. Heron, A.S. Hoey, M.O. Hoogenboom, G. Liu, et al., Global warming transforms coral reef assemblages, *Nature* 556 (7702) (2018) 492–496.
- [5] A.P. Raman, M. Abou Anoma, L. Zhu, E. Rephaeli, S. Fan, Passive radiative cooling below ambient air temperature under direct sunlight, *Nature* 515 (7528) (2014) 540–544.
- [6] Z. Chen, L. Zhu, A. Raman, S. Fan, Radiative cooling to deep sub-freezing temperatures through a 24-h day–night cycle, *Nature Commun.* 7 (1) (2016) 1–5.
- [7] X. Zhang, Metamaterials for perpetual cooling at large scales, *Science* 355 (6329) (2017) 1023–1024.
- [8] A.R. Gentle, G.B. Smith, A subambient open roof surface under the Mid-Summer sun, *Adv. Sci.* 2 (9) (2015) 1500119.
- [9] E. Rephaeli, A. Raman, S. Fan, Ultrabroadband photonic structures to achieve high-performance daytime radiative cooling, *Nano Lett.* 13 (4) (2013) 1457–1461.
- [10] C. Granqvist, T. Eriksson, Materials for radiative cooling to low temperatures, in: *Materials Science for Solar Energy Conversion Systems*, Elsevier, 1991, pp. 168–203.
- [11] D. Zhao, A. Aili, Y. Zhai, J. Lu, D. Kidd, G. Tan, X. Yin, R. Yang, Subambient cooling of water: toward real-world applications of daytime radiative cooling, *Joule* 3 (1) (2019) 111–123.
- [12] X. Yin, R. Yang, G. Tan, S. Fan, Terrestrial radiative cooling: Using the cold universe as a renewable and sustainable energy source, *Science* 370 (6518) (2020) 786–791.
- [13] D. Li, X. Liu, W. Li, Z. Lin, B. Zhu, Z. Li, J. Li, B. Li, S. Fan, J. Xie, et al., Scalable and hierarchically designed polymer film as a selective thermal emitter for high-performance all-day radiative cooling, *Nature Nanotechnol.* 16 (2) (2021) 153–158.
- [14] X. Xue, M. Qiu, Y. Li, Q. Zhang, S. Li, Z. Yang, C. Feng, W. Zhang, J.-G. Dai, D. Lei, et al., Creating an eco-friendly building coating with smart subambient radiative cooling, *Adv. Mater.* 32 (42) (2020) 1906751.
- [15] J. Mandal, Y. Yang, N. Yu, A.P. Raman, Paints as a scalable and effective radiative cooling technology for buildings, *Joule* 4 (7) (2020) 1350–1356.
- [16] Y. Zhai, Y. Ma, S.N. David, D. Zhao, R. Lou, G. Tan, R. Yang, X. Yin, Scalable-manufactured randomized glass-polymer hybrid metamaterial for daytime radiative cooling, *Science* 355 (6329) (2017) 1062–1066.
- [17] J. Mandal, Y. Fu, A.C. Overvig, M. Jia, K. Sun, N.N. Shi, H. Zhou, X. Xiao, N. Yu, Y. Yang, Hierarchically porous polymer coatings for highly efficient passive daytime radiative cooling, *Science* 362 (6412) (2018) 315–319.
- [18] I. Lienhard, H. John, *A Heat Transfer Textbook*, phlogiston Press, 2005.
- [19] T. Li, Y. Zhai, S. He, W. Gan, Z. Wei, M. Heidarinejad, D. Dalgo, R. Mi, X. Zhao, J. Song, et al., A radiative cooling structural material, *Science* 364 (6442) (2019) 760–763.
- [20] L. Cai, J. Wang, J. Peng, Z. Wu, X. Tan, Observation of the degradation of three types of plastic pellets exposed to UV irradiation in three different environments, *Sci. Total Environ.* 628 (2018) 740–747.
- [21] A.D. Vethaak, J. Legler, Microplastics and human health, *Science* 371 (6530) (2021) 672–674.
- [22] D.M. Mitrano, P. Wick, B. Nowack, Placing nanoplastics in the context of global plastic pollution, *Nature Nanotechnol.* 16 (5) (2021) 491–500.
- [23] D. Cressey, Microplastics damage oyster fertility, *Nat. News* (2016).
- [24] C.G. Björndal, Microbial degradation of waterlogged archaeological wood, *J. Cult. Herit.* 13 (3) (2012) S118–S122.
- [25] U.G. Wegst, H. Bai, E. Saiz, A.P. Tomsia, R.O. Ritchie, Bioinspired structural materials, *Nature Mater.* 14 (1) (2015) 23–36.
- [26] H.L. Jang, G.B. Zheng, J. Park, H.D. Kim, H.-R. Baek, H.K. Lee, K. Lee, H.N. Han, C.-K. Lee, N.S. Hwang, et al., In vitro and in vivo evaluation of whitlockite biocompatibility: Comparative study with Hydroxyapatite and  $\beta$ -Tricalcium Phosphate, *Adv. Healthcare Mater.* 5 (1) (2016) 128–136.
- [27] K. Zhang, Y. Zhou, C. Xiao, W. Zhao, H. Wu, J. Tang, Z. Li, S. Yu, X. Li, L. Min, et al., Application of hydroxyapatite nanoparticles in tumor-associated bone segmental defect, *Sci. Adv.* 5 (8) (2019) eaax6946.
- [28] L. Cheng, H. Wu, J. Li, H. Zhao, L. Wang, Polydopamine modified ultrathin hydroxyapatite nanosheets for anti-corrosion reinforcement in polymeric coatings, *Corros. Sci.* 178 (2021) 109064.
- [29] H. Nosrati, R.S. Mamooory, D.Q.S. Le, C.E. Bünger, R.Z. Emameh, F. Dabir, Gas injection approach for synthesis of hydroxyapatite nanorods via hydrothermal method, *Mater. Charact.* 159 (2020) 110071.
- [30] M.-s. Yang, C. Tian, C.-r. Han, G.-z. Zhao, Hierarchical self-assembled hollow hydroxyapatite flower microspheres containing terpene functional groups for efficient drug loading and pH-responsive drug release, *Ceram. Int.* 44 (17) (2018) 20913–20920.
- [31] F.-F. Chen, Y.-J. Zhu, F. Chen, L.-Y. Dong, R.-L. Yang, Z.-C. Xiong, Fire alarm wallpaper based on fire-resistant hydroxyapatite nanowire inorganic paper and graphene oxide thermosensitive sensor, *ACS Nano* 12 (4) (2018) 3159–3171.
- [32] Z.-C. Xiong, R.-L. Yang, Y.-J. Zhu, F.-F. Chen, L.-Y. Dong, Flexible hydroxyapatite ultralong nanowire-based paper for highly efficient and multifunctional air filtration, *J. Mater. Chem. A* 5 (33) (2017) 17482–17491.
- [33] F.-F. Chen, Y.-J. Zhu, Z.-C. Xiong, T.-W. Sun, Y.-Q. Shen, Highly flexible superhydrophobic and fire-resistant layered inorganic paper, *ACS Appl. Mater. Interfaces* 8 (50) (2016) 34715–34724.
- [34] Y. Chen, B. Dang, J. Fu, C. Wang, C. Li, Q. Sun, H. Li, Cellulose-based hybrid structural material for radiative cooling, *Nano Lett.* 21 (1) (2020) 397–404.
- [35] T. Wang, Y. Wu, L. Shi, X. Hu, M. Chen, L. Wu, A structural polymer for highly efficient all-day passive radiative cooling, *Nature Commun.* 12 (1) (2021) 1–11.
- [36] X. Li, J. Peoples, P. Yao, X. Ruan, Ultrawhite BaSO<sub>4</sub> paints and films for remarkable daytime subambient radiative cooling, *ACS Appl. Mater. Interfaces* 13 (18) (2021) 21733–21739.
- [37] D. Lee, M. Go, S. Son, M. Kim, T. Badloe, H. Lee, J.K. Kim, J. Rho, Sub-ambient daytime radiative cooling by silica-coated porous anodic aluminum oxide, *Nano Energy* 79 (2021) 105426.
- [38] S. Ng, J. Guo, J. Ma, S.C.J. Loo, Synthesis of high surface area mesostructured calcium phosphate particles, *Acta Biomater.* 6 (9) (2010) 3772–3781.
- [39] Z.-C. Xiong, Y.-J. Zhu, D.-D. Qin, R.-L. Yang, Flexible salt-rejecting photothermal paper based on reduced graphene oxide and hydroxyapatite nanowires for high-efficiency solar energy-driven vapor generation and stable desalination, *ACS Appl. Mater. Interfaces* 12 (29) (2020) 32556–32565.

- [40] Y. Tian, H. Shao, X. Liu, F. Chen, Y. Li, C. Tang, Y. Zheng, Superhydrophobic and recyclable cellulose-fiber-based composites for high-efficiency passive radiative cooling, *ACS Appl. Mater. Interfaces* 13 (19) (2021) 22521–22530.
- [41] X. Wang, X. Liu, Z. Li, H. Zhang, Z. Yang, H. Zhou, T. Fan, Scalable flexible hybrid membranes with photonic structures for daytime radiative cooling, *Adv. Funct. Mater.* 30 (5) (2020) 1907562.
- [42] X. Wang, Q. Liu, S. Wu, B. Xu, H. Xu, Multilayer polypyrrole nanosheets with self-organized surface structures for flexible and efficient solar-thermal energy conversion, *Adv. Mater.* 31 (19) (2019) 1807716.
- [43] B. Xiang, R. Zhang, Y. Luo, S. Zhang, L. Xu, H. Min, S. Tang, X. Meng, 3D porous polymer film with designed pore architecture and auto-deposited SiO<sub>2</sub> for highly efficient passive radiative cooling, *Nano Energy* 81 (2021) 105600.
- [44] Y. Tian, X. Liu, A. Ghanekar, Y. Zheng, Scalable-manufactured metal-insulator-metal based selective solar absorbers with excellent high-temperature insensitivity, *Appl. Energy* 281 (2021) 116055.
- [45] Y. Tian, L. Qian, X. Liu, A. Ghanekar, J. Liu, T. Thundat, G. Xiao, Y. Zheng, High-temperature and abrasion-resistant metal-insulator-metal metamaterials, *Mater. Today Energy* 21 (2021) 100725.
- [46] K.M. Mayer, J.H. Hafner, Localized surface plasmon resonance sensors, *Chem. Rev.* 111 (6) (2011) 3828–3857.



**Mr. Yanpei Tian** received his Ph.D. degree from Northeastern University in 2021 and his B.Eng. degree from Harbin Engineering University in 2015. Currently, he is a Postdoc in the X-Thermal Lab at Huazhong University of Science and Technology. His current research includes photonic manipulation for applications on radiative cooling and selective solar absorbers.



**Mrs. Xiaojie Liu** received her B.Eng. degree from Harbin Engineering University in 2016. Currently, she is a Ph.D. student in the Nano Energy Lab at Northeastern University, Boston, US. Her current research includes photothermal conversion for solar-driven evaporation.



**Mr. Ziqi Wang** received his B.Eng. and M.S. in Energy Systems from Nanjing University of Science and Technology, Nanjing, China, in 2018, and Northeastern University, Boston, in 2021, respectively. Currently, he is a Ph.D. student of Mechanical Engineering from North Carolina State University. His current interests mainly focus on Time-domain thermoreflectance (TDTR) method for multiple thermophysical properties determination in nano-scale layered structures and thermal transport in intercalated two-dimensional materials.



**Mr. Jiansheng Li** received his B.Eng. degree from Anhui University of Science and Technology in 2018 and received his M.Eng. degree in Mechanical Engineering at Northeastern University, Boston, US in 2021. Now, he is a senior engineer at Schneider Electric (China) Co., Ltd.



**Ying Mu** received her B.Eng from Hefei University of Technology. Currently, she is a Ph.D. student of materials science in Northeastern University, Boston, US. Ying's research is focused on blending processes between 1D nano-materials and polymers.



**Ms. Shiyu Zhou** received her B.S. degree from Nanjing University (NJU), Nanjing, China, in 2018. Currently, she is a Ph.D. student of Physics at Brown University and got her M.S. degree there in 2021. Her current research interests mainly focus on magnetic sensors and magnetic materials.



**Mr. Fangqi Chen** received his B.Eng. degree from Fudan University, Shanghai, China, in 2017. He received his M.Eng. degree from Boston University, USA, in 2019. Currently, he is a Ph.D. student of Nano Energy Lab from Northeastern University, USA. His current research interest mainly focuses on reconfigurable metamaterials induced dynamic photonic manipulation and near-field radiative heat transfer.



**Dr. Marilyn Minus** is a Professor and Chair for the Department of Mechanical and Industrial Engineering at Northeastern University in Boston, MA, USA. Prior to joining the faculty at Northeastern she completed her Ph.D. at Georgia Institute of Technology in the School of Polymer, Textile, and Fiber Engineering. Dr. Minus' research interests concern the structure-property relationships in nano-composites. Dr. Minus' research is also focused in the area of fabrication and characterization of advanced high-performance polymer nano-composites.



**Dr. Gang Xiao** is Professor of Physics and Professor of Engineering at Brown University, also serving as the Chair of the Physics Department. He pursued his doctoral and postdoctoral studies at Johns Hopkins University. He is a Fellow of the American Physical Society and an Alfred P. Sloan Fellow. He conducts research in condensed matter physics, novel electronic and magnetic materials.



**Dr. Yi Zheng** is an Associate Professor in the Department of Mechanical and Industrial Engineering at Northeastern University. He obtained his Ph.D. and M.S. degrees at Columbia University (New York, NY, USA) and B.E. degree at Tsinghua University (Beijing, China). He leads a research group featuring nano energy from multiple disciplines in materials science, physics, and engineering.